Asociación Argentina
de Mecánica Computacional

Mecánica Computacional Vol XXX, págs. 2877-2890 (artículo completo)
Oscar Möller, Javier W. Signorelli, Mario A. Storti (Eds.)
Rosario, Argentina, 1-4 Noviembre 2011

INTEGRATED FLUID-FLOW AND TIME-LAPSE SEISMICS TO MONITOR CARBON DIOXIDE SEQUESTRATION

Gabriela B. Savioli[a] **and Juan E. Santos**[b,c]

[a]*Laboratorio de Ingeniería de Reservorios, Instituto del Gas y del Petróleo and Dto. de Ing. Química, Facultad de Ingeniería, Universidad de Buenos Aires, Av. Las Heras 2214 Piso 3 C1127AAR Buenos Aires, Argentina, gsavioli@di.fcen.uba.ar*

[b]*CONICET, Instituto del Gas y del Petróleo, Facultad de Ingeniería, Universidad de Buenos Aires, Av. Las Heras 2214 Piso 3 C1127AAR Buenos Aires, Argentina*

[c]*Department of Mathematics, Purdue University, 150 N. University Street, West Lafayette, Indiana, 47907-2067, USA, santos@math.purdue.edu*

Keywords: CO_2 Sequestration, Finite Elements, Wave Propagation

Abstract. Carbon Dioxide (CO_2) sequestration into geologic formations is a means of mitigating greenhouse effect. In this work we present numerical simulation techniques to model and monitor CO_2 sequestration. For that purpose we integrate numerical simulators of CO_2-brine flow and seismic wave propagation (time-lapse seismics). The simultaneous flow of brine and CO_2 is modeled applying the Black-Oil formulation for two phase flow in porous media, which uses the Pressure-Volume-Temperature (PVT) behavior as a simplified thermodynamic model. Seismic wave propagation uses a simulator based on a space-frequency domain formulation of the viscoelastic wave equation. In this formulation, the complex and frequency dependent coefficients represent the attenuation and dispersion effect suffered by seismic waves travelling in fluid-saturated heterogeneous porous formations. The spatial discretization is achieved employing a nonconforming finite element space to represent the displacement vector. Numerical examples of CO_2 injection and time-lapse seismics in the Utsira formation at the Sleipner field are analyzed, including the presence of shale seals and fractures. The results of the simulations show the capability of the proposed methodology to monitor the spatial distribution of CO_2 after injection.

1 INTRODUCTION

Fossil-fuel combustion generates carbon dioxide (CO_2), which is mainly discharged into the atmosphere, increasing its temperature (greenhouse effect). To minimize this effect, an interesting alternative is to inject CO_2 into a target geologic formation, such as aging oil fields, ocean water, reservoirs and saline aquifers (Arts et al., 2008). Among these options, saline aquifers have the advantage of their large volume and their common occurrence in nature. The injection is performed at depths typically greater than 1000 m where pressure and temperature are above the critical point for CO_2 (31.6C, 7.38 MPa).

The CO_2 injection operation at the Sleipner gas field in the North Sea , operated by Statoil and the Sleipner partners, is the world first industrial scale CO_2 injection project designed specifically as a greenhouse gas mitigation measure. Injection started in 1996 and is planned to continue for about twenty years, at a rate of about one million tonnes per year (Arts et al., 2008)-(Chadwick et al., 2005). CO_2 separated from natural gas produced at Sleipner is currently being injected into the Utsira Sand, a saline aquifer some 26000 km^2 in area.

Up to now, very little is known about the effectiveness of CO_2 storage over long periods of time. Therefore, numerical modeling of CO_2 injection and seismic monitoring is an important tool to understand the long term behavior of CO_2 after injection and to test the effectiveness of CO_2 sequestration. Recent papers (Santos et al., 2008), (Carcione and Picotti, 2006) successfully apply seismic modeling for monitoring the spatio-temporal distribution of CO_2 using synthetic generated CO_2 saturation fields.

In this work we integrate numerical simulators of CO_2-brine flow and seismic wave propagation. The simultaneous flow of brine and CO_2 is modeled applying the Black-Oil formulation for two phase flow in porous media, which uses the PVT data as a simplified thermodynamic model.

Seismic monitoring is modeled using an isotropic viscoelastic model to represent the propagation of waves in the subsurface. The complex plane-wave and shear modulus are determined taking into account the heterogeneities in the fluid and solid phases and using a continuous superposition of Zener model to represent the viscoelastic behavior of the material (Liu et al., 1976).

Numerical examples of CO_2 injection and time-lapse seismics are analyzed to show the capability of the proposed methodology to identify the horizontal and vertical saturation distribution of CO2.

The final objective is to test that underground storage is a safe and verifiable technology in the long term.

2 THE BLACK-OIL FORMULATION OF TWO-PHASE FLOW IN POROUS MEDIA

The simultaneous flow of brine and CO_2 in porous media is described by the well-known Black-Oil formulation applied to two-phase, two component fluid flow (Aziz and Settari, 1985). We represent the brine (subindex b) by the oil phase and the CO_2 (subindex $CO2$) by the gas phase. In this way, CO_2 component may dissolve in the brine phase but the brine is not allowed to vaporize into the CO_2 phase. The differential equations are obtained by combining the mass conservation equations with Darcy's empirical law.

The mass conservation equations are:

- For the CO_2 component,

$$-\nabla\cdot(\rho_{CO2}\,\hat{v}_{CO2}+C_{CO2,b}\,\rho_b\,\hat{v}_b)+q_{CO2}=\frac{\partial\Big[\phi\,(\rho_{CO2}S_{CO2}+C_{CO2,b}\,\rho_b\,S_b)\Big]}{\partial t}, \quad (1)$$

- For the brine component,

$$-\nabla\cdot(C_{b,b}\,\rho_b\,\hat{v}_b)+q_b=\frac{\partial\Big[\phi(C_{b,b}\,\rho_b\,S_b)\Big]}{\partial t}, \quad (2)$$

where ρ is density, $\hat{v}$ is Darcy velocity, S is saturation, q mass rate of injection per unit volume and ϕ is porosity. $C_{CO2,b}$, $C_{b,b}$ are the mass fractions of CO_2 and brine in the brine phase, respectively. In the Black-Oil formulation these fractions are computed using a simplified thermodynamic model (PVT data), as

$$C_{CO2,b}=\frac{R_s\,\rho_{CO2}\,B_{CO2}}{B_b\,\rho_b} \quad (3)$$

$$C_{b,b}=\frac{\rho_b^{SC}}{B_b\rho_b} \quad (4)$$

R_s, B_{CO2} and B_b are PVT data, defined as

- $R_s=\dfrac{V_{dCO2}^{SC}}{V_b^{SC}}$, CO_2 solubility in brine;
- $B_{CO2}=\dfrac{V_{CO2}^{res}}{V_{CO2}^{SC}}$, CO_2 formation volume factor;
- $B_b=\dfrac{(V_{dCO2}^{res}+V_b^{res})}{V_b^{SC}}$, brine formation volume factor;

where V_{CO2}^{res}, V_b^{res} and V_{dCO2}^{res} are the volume of CO_2, brine and dissolved CO_2 in brine at reservoir conditions; and V_{CO2}^{SC}, V_b^{SC} and V_{dCO2}^{SC} are the volume of CO_2, brine and dissolved CO_2 in brine at standard conditions, respectively. Also, ρ_b^{SC} and ρ_{CO2}^{SC} are the CO_2 and brine densities at standard conditions.

The empirical Darcy‘s Law gives the momentum balance for the fluids,

$$\hat{v}_{CO2}=-\underline{k}\frac{k_{rCO2}}{\mu_{CO2}}(\nabla p_{CO2}-\rho_{CO2}g\nabla D), \quad (5)$$

$$\hat{v}_b=-\underline{k}\frac{k_{rb}}{\mu_b}(\nabla p_b-\rho_b g\nabla D), \quad (6)$$

where p_{CO2}, p_b are the fluid pressures and $\underline{k}$ is the absolute permeability. Also, for $\beta=CO2,b$, the funcions $k_{r\beta}$ and μ_β are the relative permeability and viscosity of the β-phase, respectively.

Replacing (3)-(6) in (1)-(2) and dividing by ρ_{CO2}^{SC} and ρ_b^{SC}, the following nonlinear system of partial differential equation is obtained,

$$\nabla \cdot (\underline{k}(\frac{k_{rCO2}}{B_{CO2}\mu_{CO2}}(\nabla p_{CO2} - \rho_{CO2} g \nabla D) + \frac{R_s k_{rb}}{B_b \mu_b}(\nabla p_b - \rho_b g \nabla D))) + \frac{q_{CO2}}{\rho^{SC}_{CO2}} = \frac{\partial\left[\phi\left(\frac{S_{CO2}}{B_{CO2}} + \frac{R_s S_b}{B_b}\right)\right]}{\partial t}, \tag{7}$$

$$\nabla \cdot (\underline{k}\frac{k_{rb}}{B_b \mu_b}(\nabla p_b - \rho_b g \nabla D) + \frac{q_b}{\rho^{SC}_b} = \frac{\partial\left[\phi \frac{S_b}{B_b}\right]}{\partial t}. \tag{8}$$

Two algebraic equations relating the saturations and pressures, complete the system:

$$S_b + S_{CO2} = 1, \qquad p_{CO2} - p_b = P_C(S_b), \tag{9}$$

where P_C is the capillary pressure.

The unknowns for the Black-Oil model are the fluid pressures p_{CO2}, p_b and the saturations S_{CO2}, S_b for the CO_2 and brine phases.

R_s and B_b can be expressed in terms of the equilibrium properties obtained from an equation of state (Hassanzadeh et al., 2008)-(Spycher and Pruess, 2005):

- $R_s = \dfrac{\tilde{\rho}^{SC}_b \chi_{CO2}}{\tilde{\rho}^{SC}_{CO2}(1 - \chi_{CO2})}$
- $B_b = \dfrac{\rho^{SC}_b}{\rho_b(1 - \omega_{CO2})}$

where $\tilde{\rho}^{SC}_b$ and $\tilde{\rho}^{SC}_{CO2}$ are the brine and CO_2 molar density at standard conditions; and χ_{CO2} and ω_{CO2} are the CO_2 mole fraction and the CO_2 mass fraction in the brine phase. This conversion from compositional data from equations of state into the black-oil PVT data is performed applying an algorithm developed by Hassanzadeh et al (Hassanzadeh et al., 2008).

The numerical solution was obtained employing the public domain software BOAST (Fanchi, 1997). BOAST solves the differential equations using IMPES (IMplicit Pressure Explicit Saturation), a semi-implicit finite difference technique (Savioli and Bidner, 2005).

3 A VISCOELASTIC MODEL FOR WAVE PROPAGATION

The propagation of waves in porous media is described using an equivalent viscoelastic model that takes into account the dispersion and attenuation effects due to the presence of heterogeneities in the fluid and solid phase properties.

The equation of motion in a 2D isotropic viscoelastic domain Ω with boundary $\partial\Omega$ can be stated in the space-frequency domain as

$$-\omega^2 \rho u - \nabla \cdot \sigma(u) = f(x, \omega), \quad \Omega \tag{10}$$

$$-\sigma(u)\nu = i\omega \mathcal{D} u, \quad \partial\Omega, \tag{11}$$

where $u = (u_x, u_y)$ is the displacement vector. Here ρ is the bulk density and (11) is a first-order absorbing boundary condition using the positive definite matrix $\mathcal{D}$, which definition is given in (Ha et al., 2002).

The stress tensor $\sigma(u)$ is defined in the space-frequency domain by

$$\sigma_{jk}(u) = \lambda_G(\omega)\nabla \cdot u\delta_{jk} + 2N(\omega)\varepsilon_{jk}(u), \quad \Omega, \tag{12}$$

where $\varepsilon_{jk}(u)$ denotes the strain tensor and δ_{jk} is the Kroenecker delta.

The coefficient N in (12) is the shear modulus of the dry matrix, while the Lamé coefficient is $\lambda_G = K_G - \frac{2}{3}\mu$ in 3D and $\lambda_G = K_G - \mu$ in 2D. K_G is the Gassmann's undrained bulk modulus, computed as follows:

$$K_G = K_m + \alpha^2 K_{av}$$
$$\alpha = 1 - \frac{K_m}{K_s},$$
$$K_{av} = \left[\frac{\alpha - \phi}{K_s} + \frac{\phi}{K_f}\right]^{-1}.$$

where

- K_m: bulk modulus of the dry matrix
- K_s: bulk modulus of the solid grains
- K_f: bulk modulus of the saturant fluid

To introduce viscoelasticity we use the *correspondence principle* stated by M. Biot (Biot, 1962, 1956), i.e. we replace the real poroelastic coefficients in the constitutive relations by complex frequency dependent poroviscoelastic moduli satisfying the same relations as in the elastic case, with some necessary thermodynamic restrictions. In this work we use the linear viscoelastic model presented in (Liu et al., 1976) to make the undrained bulk modulus K_G and the shear modulus N complex and frequency dependent. Thus, we take

$$K_G(\omega) = \frac{K_G^{re}}{R_{K_G}(\omega) - iT_{K_G}(\omega)}, \qquad N(\omega) = \frac{N^{re}}{R_N(\omega) - iT_N(\omega)}, \tag{13}$$

where $\omega = 2\pi f$: angular frequency and K_G^{re}, N^{re} are the relaxed Gassmann's and shear modulus.

The functions R_l and T_l, $l = K_c, N$, associated with a continuous spectrum of relaxation times, characterize the viscoelastic behaviour and are given by (Liu et al., 1976)

$$R_l(\omega) = 1 - \frac{1}{\pi\widehat{Q}_l}\ln\frac{1+\omega^2 T_{1,l}^2}{1+\omega^2 T_{2,l}^2}, \qquad T_l(\omega) = \frac{2}{\pi\widehat{Q}_l}\tan^{-1}\frac{\omega(T_{1,l} - T_{2,l})}{1+\omega^2 T_{1,l}T_{2,l}}.$$

The model parameters $\widehat{Q}_l$, $T_{1,l}$ and $T_{2,l}$ are taken such that the quality factors $Q_l(\omega) = T_l/R_l$ are approximately equal to $\widehat{Q}_l$ in the range of frequencies where the equations are solved, which makes this model convenient for geophysical applications.

The approximate solution of (10) with the boundary conditions (11) is obtained using a finite element procedure employing a uniform partition $\mathcal{T}^h$ of the computational domain Ω into square subdomains $\Omega_m, m = 1, \cdots, M$ of side length h. To approximate each component of the solid displacement vector we employed the nonconforming finite element space defined in (Douglas, Jr. et al., 1999), since it generates less numerical dispersion than the standard bilinear elements (Zyserman et al., 2003). It can be demonstrated that the error associated with this numerical procedure measured in the energy norm is of order h (Ha et al., 2002).

4 THE ITERATIVE DOMAIN DECOMPOSITION ALGORITHM

4.1 Weak Formulation

We proceed to formulate the variational form for viscoelastic waves: Find $\widehat{u} \in [H^1(\Omega)]^N$ such that

$$-(\rho\omega^2\widehat{u},\varphi) + \sum_{pq}(\tau_{pq}(\widehat{u}),\varepsilon_{pq}(\varphi)) + i\omega\,\langle \mathcal{A}\widehat{u},\varphi\rangle_\Gamma = (\widehat{f},\varphi), \quad \varphi \in [H^1(\Omega)]^N.$$

Here $(f,g) = \int_\Omega f\overline{g}\,dx$ and $\langle f,\overline{g}\rangle = \int_\Gamma f\overline{g}\,d\Gamma$ denote the complex $[L^2(\Omega)]^N$ and $[L^2(\Gamma)]^N$ inner products. Also, $H^1(\Omega)$ denotes the usual Sobolev space of functions in $L^2(\Omega)$ with first derivatives in $L^2(\Omega)$.

4.2 Finite Element Method

The nonconforming finite element space used in this paper was first described in (Douglas, Jr. et al., 1999). For $h > 0$, let $\mathcal{T}_h$ be a quasiregular partition of $\overline{\Omega}$ such that $\overline{\Omega} = \cup_{j=1}^J \overline{\Omega}_j$ with Ω_j being N-rectangles of diameter bounded by h. Set $\Gamma_j = \partial\Omega \cap \partial\Omega_j$ and $\Gamma_{jk} = \Gamma_{kj} = \partial\Omega_j \cap \partial\Omega_k$, we denote by ξ_j and ξ_{jk} the centroids of Γ_j and Γ_{jk}, respectively.

We consider a nonconforming finite element space constructed using the following reference rectangular element

$$\widehat{R} = [-1,1]^2 \qquad S_2(\widehat{R}) = \text{Span}\left\{\frac{1}{4} \pm \frac{1}{2}x - \frac{3}{8}\left((x^2 - \frac{5}{3}x^4) - (y^2 - \frac{5}{3}y^4)\right),\right.$$
$$\left.\frac{1}{4} \pm \frac{1}{2}y + \frac{3}{8}\left((x^2 - \frac{5}{3}x^4) - (y^2 - \frac{5}{3}y^4)\right)\right\}.$$

The four degrees of freedom associated with $S_2(\widehat{R})$ are the values at the mid points of the faces of $\widehat{R}$, i.e., the values at the nodal points $a_1 = (-1,0), a_2 = (0,-1), a_3 = (1,0)$ and $a_4 = (0,1)$. For example the basis function $\psi_1(x,y) = \frac{1}{4} - \frac{1}{2}x - \frac{3}{8}\left((x^2 - \frac{5}{3}x^4) - (y^2 - \frac{5}{3}y^4)\right)$ is such that $\psi_1(a_1) = 1$ and $\psi_1(a_j) = 0, j = 2,3,4$.

One of the main advantages of using nonconforming elements to solve wave propagation phenomena is that the amount of information exchanged among processors in a domain decomposition iterative procedure is considerable reduced as compared to the case when conforming elements are employed. Another property of the nonconforming elements is that it is possible to obtain an estimate on the speed of convergence of the iterative domain decomposition procedure as a function of the mesh size h.

Set $NC_j^h = S_N(\Omega_j),\ N = 2,3$ and define a nonconforming finite element space in the following manner

$$NC^h = \left\{v \mid v_j : = v\mid_{\Omega_j} \in NC_j^h, j = 1,\ldots,J; \quad v_j(\xi_{jk}) = v_k(\xi_{jk}),\ \forall\{j,k\}\right\}.$$

The global nonconforming Galerkin procedure is defined as follows: find $\widehat{u}^h \in [NC^h]^2$ such that

$$-(\rho\omega^2\widehat{u}^h,\varphi) + \sum_{pq}(\tau_{pq}(\widehat{u}^h),\varepsilon_{pq}(\varphi)) + i\omega\left\langle\left\langle \mathcal{A}\widehat{u}^h,\varphi\right\rangle\right\rangle_\Gamma = (\widehat{f},\varphi), \quad \varphi \in [NC^h]^2.$$

Next, we will define a discrete domain decomposition iterative hybridized procedure. For this purpose, we introduce a new set $\widetilde{\Lambda}^h$ of Lagrange multipliers λ_{jk}^h associated with the stress values $-\tau(\widehat{u}_j)\nu_{jk}(\xi_{jk})$:

$$\widetilde{\Lambda}^h = \{\lambda^h \colon \lambda^h|_{\Gamma_{jk}} = \lambda_{jk}^h \in [P_0(\Gamma_{jk})]^N = [\Lambda_{jk}^h]^N\}.$$

Then, given an initial guess $\left(\widehat{u}_j^{h,0}, \lambda_{jk}^{h,0}, \lambda_{kj}^{h,0}\right) \in [NC_j^h]^N \times [\Lambda_{jk}^h]^N \times [\Lambda_{kj}^h]^N$, compute $\left(\widehat{u}_j^{h,n}, \lambda_{jk}^{h,n}\right) \in [NC_j^h]^N \times [\Lambda_{jk}^h]^N$ as the solution of the equations

$$-(\rho\omega^2\widehat{u}_j^{h,n}, \varphi)_j + \sum_{pq}(\tau_{pq}(\widehat{u}^{h,n}), \varepsilon_{pq}(\varphi))_j + i\omega \left\langle\left\langle \mathcal{A}\widehat{u}_j^{h,n}, \varphi \right\rangle\right\rangle_{\Gamma_j}$$
$$+ \sum_k \left\langle\left\langle \lambda_{jk}^{h,n}, \varphi \right\rangle\right\rangle_{\Gamma_{jk}} = (\widehat{f}, \varphi)_j, \quad \varphi \in [NC_j^h]^N, \tag{14}$$

$$\lambda_{jk}^{h,n} = -\lambda_{kj}^{h,n-1} + i\beta_{jk}[\widehat{u}_j^{h,n}(\xi_{jk}) - \widehat{u}_k^{h,n-1}(\xi_{jk})], \qquad \text{on } \Gamma_{jk}. \tag{15}$$

It can be shown that

$$\widehat{[}u^{h,n} - \widehat{u}^h]^2 \to 0 \text{ in } [L^2(\Omega)]^2 \quad \text{when} \quad n \to \infty,$$

so that in the limit the global nonconforming Galerkin approximation is obtained (Ha et al., 2002).

5 NUMERICAL EXPERIMENTS

5.1 Idealized model of the Utsira formation

To test the proposed methodology, we consider an idealized geometrical and physical domain consisting of 5 regions as shown in Figure 1. The upper 100 m is region Ω_1, a sand of permeability 60 mD and porosity 0.32. Ω_2 is a sealed shale 2 m thick, the top of the Usira formation. Regions Ω_3 and Ω_5 are the Utsira formation, of permeability 1000 mD and porosity 0.37. We assume that Ω_4 is a fractured shale seal layer within the Utsira sand.

We consider wave propagation in these poroelastic medium. The material properties of the system are given in Table 1 (Carcione et al., 2006)

Utsira Solid Matrix	Grain bulk modulus, K_s	40 GPa
	Frame bulk modulus, K_m	1.37 GPa
	shear modulus, N	0.82 GPa
	Grain density, ρ_s	2600 kg/m^3
Shale Solid Matrix	Grain bulk modulus, K_s	20 GPa
	Frame bulk modulus, K_m	7 GPa
	shear modulus, N	6 GPa
	Grain density, ρ_s	2600 kg/m^3
Water	bulk modulus, K_f	2.64 GPa
	density, ρ_f	1040 kg/m^3
	viscosity, η	3 cP
Gas	bulk modulus, K_f	25 MPa
	density, ρ_2	505 kg/m^3
	viscosity, η	0.15 cP

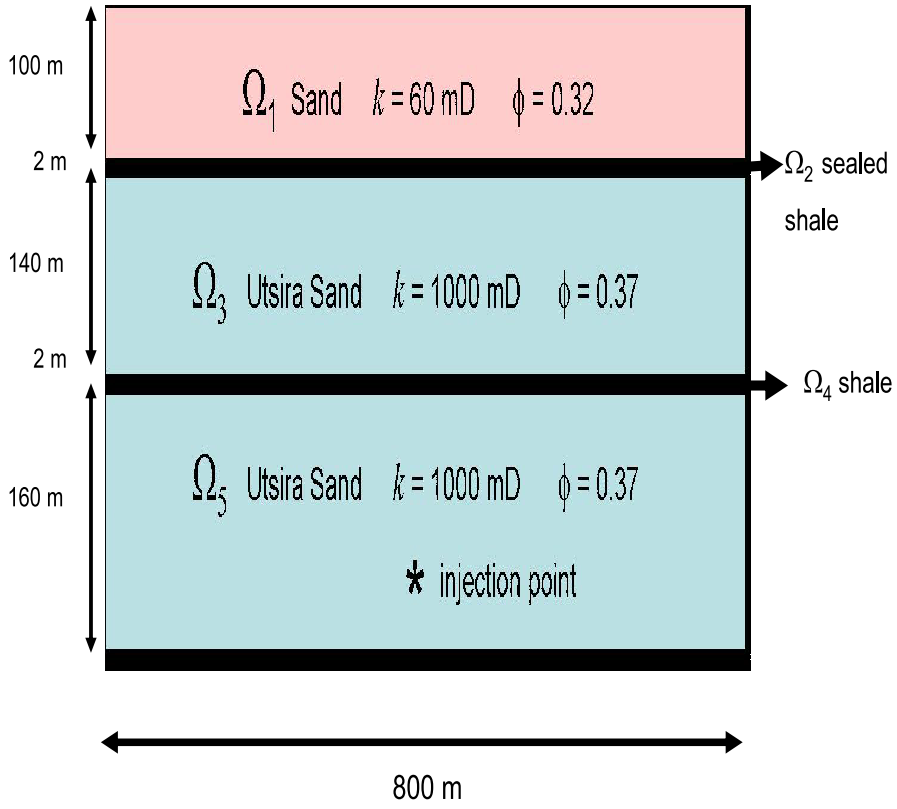

Figure 1: Idealized model of the Utsira formation. The injection point is located at x= 400 m, z= 1060 m

Table 1. Material properties of the system

It is convenient first to approximate the saturated porous medium Ω by a viscoelastic solid and use the concept of complex velocity as follows. Recall that in a viscoelastic solid, the quality factor $Q(\omega)$ is defined by the relation

$$Q(\omega) = \frac{\mathrm{Re}(v_p^2)}{\mathrm{Im}(v_p^2)},$$

where v_p is the complex compressional velocity given by

$$v_p(\omega) = \sqrt{\frac{E}{\overline{\rho}_b}}. \tag{16}$$

In (16) $\overline{\rho}_b$ is the average bulk density over Ω and $E = E(\omega) = |E|e^{i\theta}$ is the complex plane wave modulus associated with the domain Ω as defined by White (White et al., 1975). The quality factor is related to the loss angle θ by the formula

$$Q^{-1}(\omega) = \tan\theta.$$

The source function $\widehat{f}$ is a compressional point source located inside the region at x= 400 m, z= 710 m. The iterative procedure was used to find the time Fourier transforms of the displacement vectors of the solid and fluid phases for 100 equally spaced temporal frequencies in the interval $(0, 60\mathrm{Hz})$.

5.2 Injection Modeling

CO_2 is injected at a constant flow rate of 5000 SCF/d. The injection point is located at the bottom of the Utsira formation: x=400 m, z=1060 m. Results are computed applying the BOAST simulator. The evolution of CO_2 saturation distribution is illustrated in Figure 2 which shows CO_2 saturation after six months , two years, 7 years and 27 years of CO_2 injection. It can be observed that there is a CO_2 accumulation below the sealed layer Ω_4. But this seal has a fracture, so, as time increases, part of the injected fluid migrates through it. Therefore, two regions of CO_2 accumulation can be observed: one beneath Ω_4 and the other beneath the top of the Usira formation. In the BOAST simulator a seal is easily represented by assigning zero permeability values to the corresponding gridblocks. Therefore, to add a fracture, we simply replace zero permeability by a positive value (in this case 5 mD) in those gridblocks where the fracture is located.

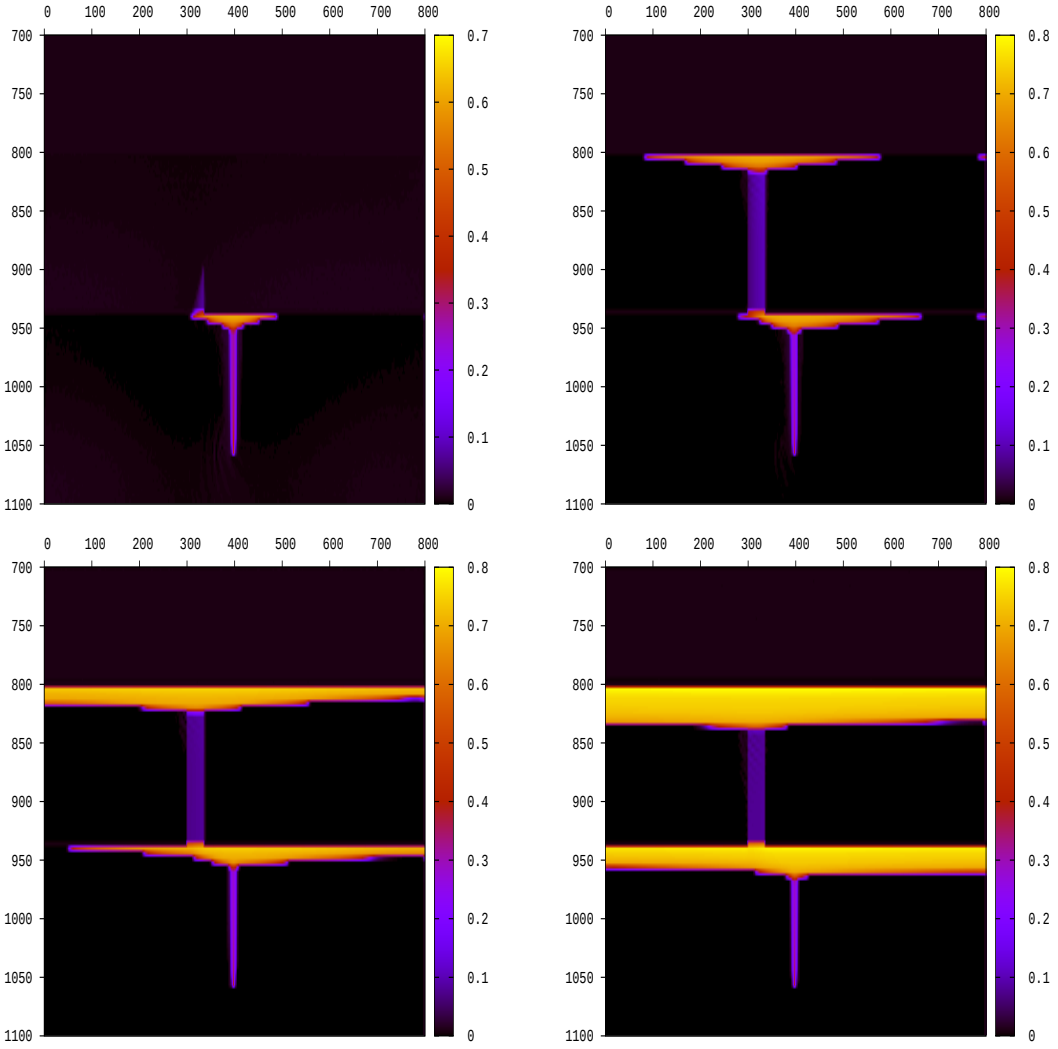

Figure 2: CO_2 saturation distribution after 6 months, 2,7 and 27 years of CO_2 injection

Figure 3 displays the distribution of P-wave phase velocity after 7 years of CO_2 injection and Figure 4 the vertical profile of the P-wave phase velocity corresponding to x= 200 m. The velocity changes due to the presence of the seals and CO_2 accumulation are clearly observed.

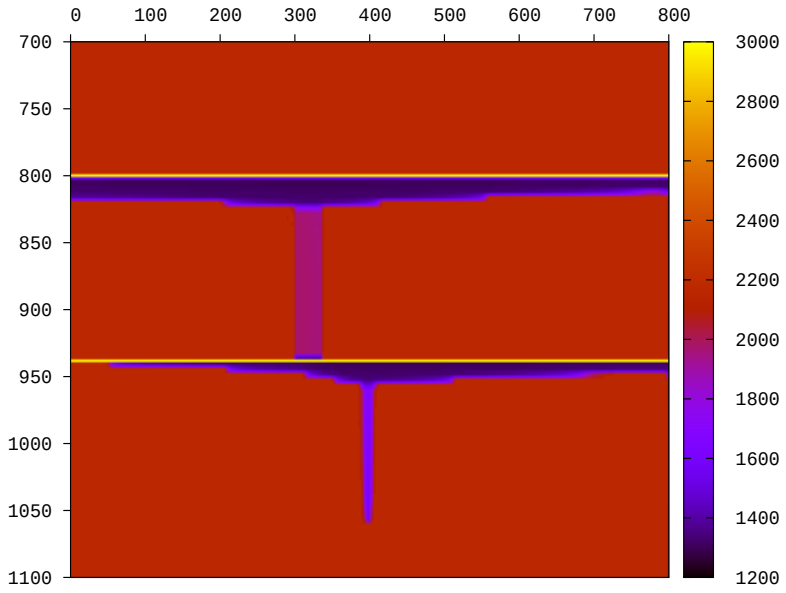

Figure 3: P-wave phase velocity after 7 years of CO_2 injection

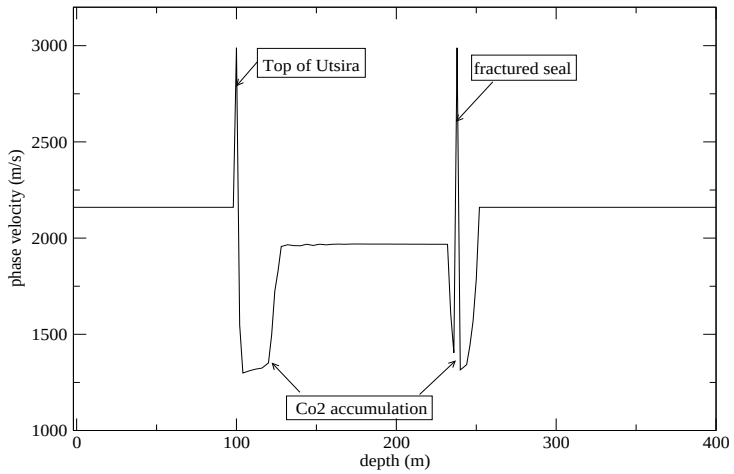

Figure 4: Vertical profile of the P-wave phase velocity after 7 years of CO_2 injection

5.2.1 Seismic Monitoring

The objective of this section is to analyze the capability of seismic monitoring to identify zones of CO_2 accumulation. With this purpose, the media is excited with a point source located at x= 400 m, z= 710m.

Figure 5 displays the vertical component of the solid phase velocity after 2 years of CO_2 injection. At 70 ms the wave front generated by the compressional point source is arriving at the top of Utsira. At 150 ms the waves generated by the point source are generated, reflected and transmitted due to the CO_2 accumulation below the top of Utsira; besides, the wave front is arriving at the thin shale layer at z = 940 m. In the same way, at 200 ms, the reflected and

transmitted waves from the CO_2 accumulation below the thin shale layer are observed.

Time histories measured near the surface are shown in Figure 6 to 9: before CO_2 injection (6); after 2 years of CO_2 injection (7), after 7 years of CO_2 injection (8) and after 27 years of CO_2 injection (9). The upper reflection in all figures is due to the direct wave coming from the point source. In Figs.7 and 8 two other reflections appear: the lower is generated by the CO_2 accumulations below the thin shale layer at depth z = 940 m. Note that this reflection is located between 300 and 800 m in 7, following the extension of CO2 accumulation for 2 years, shown in 2. The third reflection (the upper one) is due to the accumulation below the top of Utsira. In Fig.9 there are 5 reflections, the upper one corresponding to the direct wave and the others to the top and bottom of the CO2 accumulation below the shale layer at depth z=940 m and below the top of Utsira.

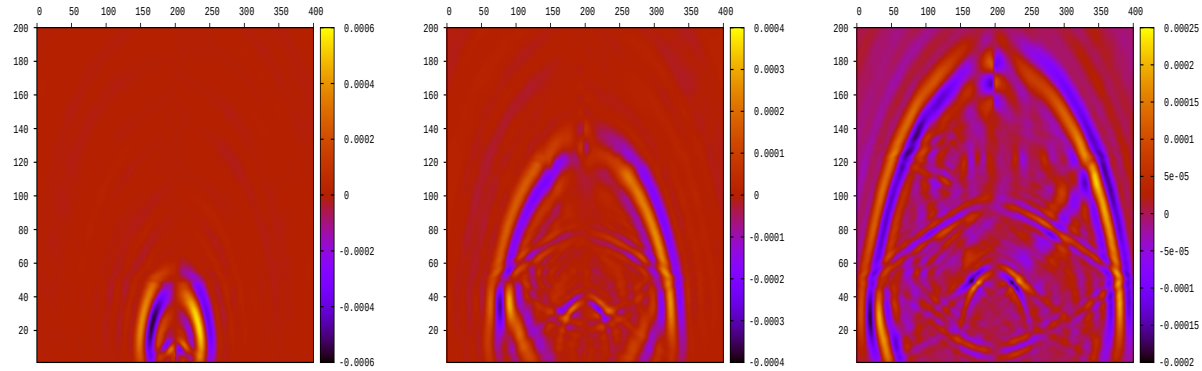

Figure 5: Vertical component of the solid phase velocity at 70, 150 and 200 ms after 2 years of CO_2 injection

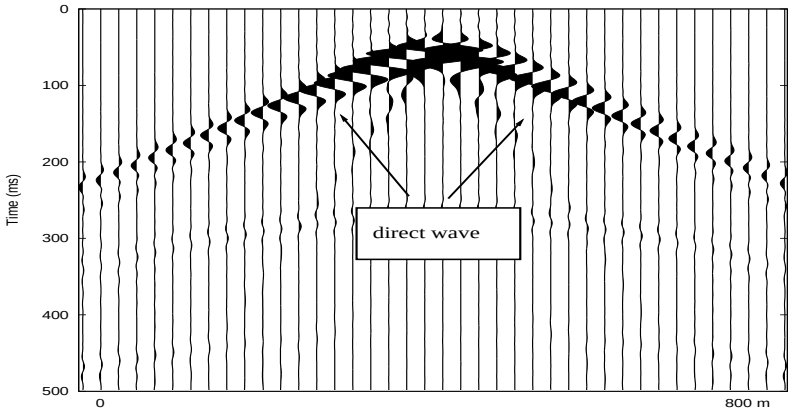

Figure 6: Time histories measured near the surface before CO_2 injection

Figure 10 displays traces of particle velocity of the solid phase after 2, 7 and 27 years of CO_2 injection. The strong arrival at about 180 ms and 240 ms correspond to the reflections due to the CO_2 accumulation beneath the top of Utsira and beneath the fractured seal, respectively.

6 CONCLUSIONS

In this work we integrate numerical simulators of CO_2-brine flow and seismic wave propagation to model and monitor CO_2 storage in saline aquifers. Numerical examples show the

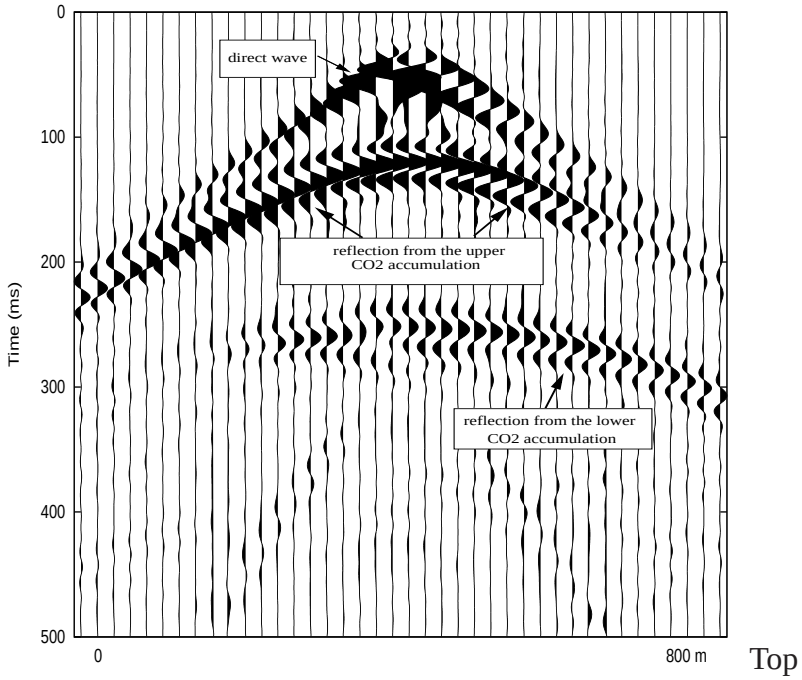

Figure 7: Time histories measured near the surface after 2 years of CO_2 injection

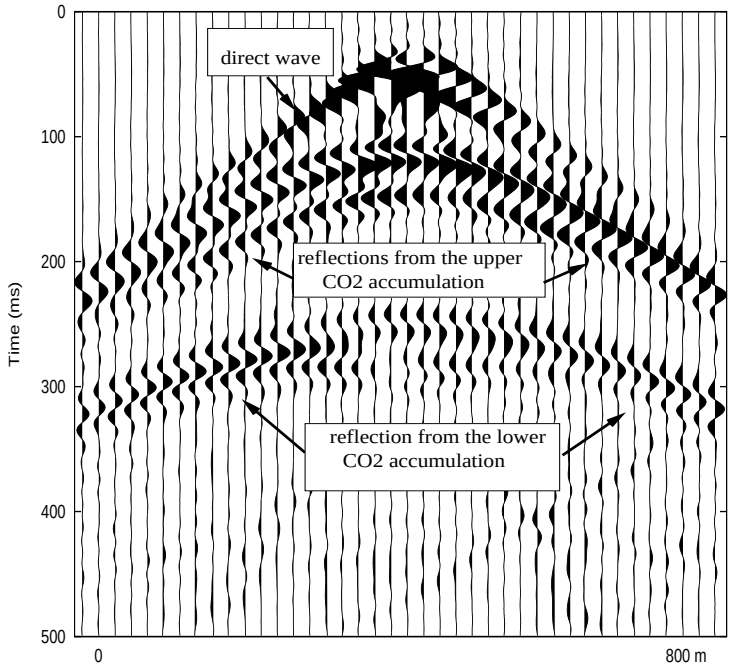

Figure 8: Time histories measured near the surface after 7 years of CO_2 injection

effectiveness of this metodology to detect the spatio-temporal distribution of CO_2. Therefore, it constitutes an important tool to monitor the migration and dispersal of the CO_2 plume and to analyze storage integrity, providing early warning should any leakage occurs.

In this work we analyzed phase velocity changes due the presence of heterogenoeus CO_2 accumulations. Future work involves the analysis of attenuation effects due to the presence of

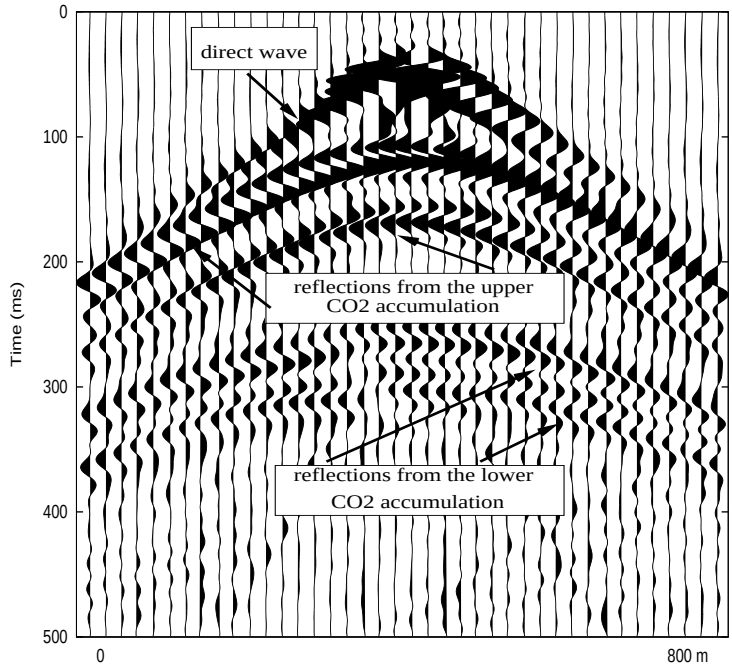

Figure 9: Time histories measured near the surface after 27 years of CO_2 injection

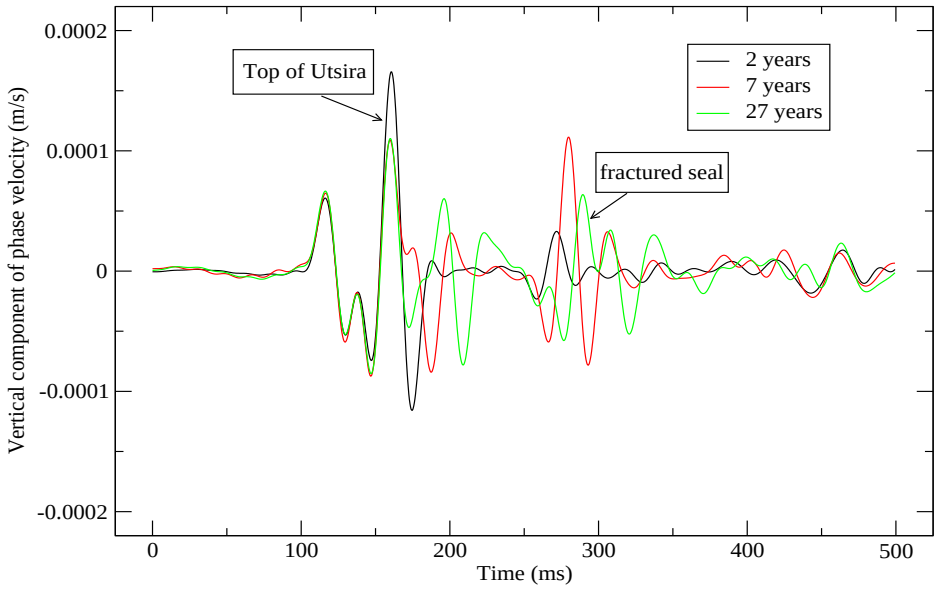

Figure 10: Traces of particle velocity of the solid phase

mesoscopic heterogeneities in the fluid and rock properties.

7 AKNOWLEDGEMENTS

This work was partially funded by CONICET, Argentina (PIP 0952)

REFERENCES

Arts R., Chadwick A., Eiken O., Thibeau S., and Nooner S. Ten years of experience of monitoring CO_2 injection in the utsira sand at sleipner, offshore norway. *First break*, 26:65–72, 2008.

Aziz K. and Settari A. *Petroleum Reservoir Simulation*. Elsevier Applied Science Publishers, Great Britain, 1985.

Biot M.A. Theory of deformation of a porous viscoelastic anisotropic solid. *J. Appl. Phys.*, 27:459–467, 1956.

Biot M.A. Mechanics of deformation and acoustic propagation in porous media. *J. Appl. Phys.*, 33:1482–1498, 1962.

Carcione J.M. and Picotti S. P-wave seismic attenuation by slow-wave diffusion:Effects of inhomogeneous rock properties. *Geophysics*, 71(3):O1–O8, 2006.

Carcione J.M., Picotti S., Gei D., and Rossi G. Physics and seismic modeling for monitoring CO_2 storage. *Pure and Applied Geophysics*, 163:175–207, 2006.

Chadwick A., Arts R., and Eiken O. 4d seismic quantification of a growing CO_2 plume at sleipner, north sea. *Dore A G and Vincent B (Eds) Petroleum Geology: North West Europe and Global Perspectives - Proc. 6th Petroleum Geology Conference*, pages 1385–1399, 2005.

Douglas, Jr. J., Santos J.E., Sheen D., and Ye X. Nonconforming Galerkin methods based on quadrilateral elements for second order elliptic problems. *RAIRO Mathematical Modelling and Numerical Analysis (M2AN)*, 33:747–770, 1999.

Fanchi J. *Principles of Applied Reservoir Simulation*. Gulf Professional Publishing Company, Houston, Texas, 1997.

Ha T., Santos J.E., and Sheen D. Nonconforming finite element methods for the simulation of waves in viscoelastic solids. *Comput. Meth. Appl. Mech. Engrg.*, 191:5647–5670, 2002.

Hassanzadeh H., Pooladi-Darvish M., Elsharkawy A., Keith D., and Leonenko Y. Predicting PVT data for CO_2-brine mixtures for black-oil simulation of CO_2 geological storage. *International Journal of Greenhouse Gas Control*, 2:65–77, 2008.

Liu H.P., Anderson D.L., and Kanamori H. Velocity dispersion due to anelasticity; implications for seismology and mantle composition. *Geophys. J. R. Astr. Soc.*, l47:41–58, 1976.

Santos J.E., Rubino J.G., and Ravazzoli C.L. Modeling mesoscopic attenuation in a highly heterogeneous biot's medium employing an equivalent viscoelastic model. *Proc. 78th Annual International Meeting SEG (Las Vegas)*, pages 2212–2215, 2008.

Savioli G. and Bidner M.S. Simulation of the oil and gas flow toward a well - a stability analysis. *Journal of Petroleum Science and Engineering*, 48:53–69, 2005.

Spycher N. and Pruess K. Co_2-h_2o mixtures in the geological sequestration of co_2. ii. partitioning in chloride brines at 12-100 c and up to 600 bar. *Geochim. Cosmochim, Acta 69*, 13:3309–3320, 2005.

White J.E., Mikhaylova N.G., and Lyakhovitskiy F.M. Low-frequency seismic waves in fluid-saturated layered rocks. *Izvestija Academy of Siences USSR, Physics of Solid Earth*, 10:654–659, 1975.

Zyserman F.I., Gauzellino P.M., and Santos J.E. Dispersion analysis of a non-conforming finite element method for the Helmholtz and elastodynamic equations. *Int. J. Numer. Meth. Engng.*, 58:1381–1395, 2003.